Science Arts & Métiers (SAM)

is an open access repository that collects the work of Arts et Métiers Institute of Technology researchers and makes it freely available over the web where possible.

This is an author-deposited version published in: https://sam.ensam.eu
Handle ID: .http://hdl.handle.net/10985/26841

To cite this version :

Qiang CHEN, Wenhui ZHAO, Ce XIAO, Zhibo YANG, George CHATZIGEORGIOU, Fodil MERAGHNI, Xuefeng CHEN - Hybrid homogenization neural networks for periodic composites - International Journal of Solids and Structures - Vol. 322, p.113622 - 2025

Any correspondence concerning this service should be sent to the repository Administrator : scienceouverte@ensam.eu

Arts et Métiers Institute of Technology

Hybrid homogenization neural networks for periodic composites

Qiang Chen [a,b], Wenhui Zhao [a,b], Ce Xiao [a,b], Zhibo Yang [a,b,*], George Chatzigeorgiou [c], Fodil Meraghni [c], Xuefeng Chen [a,b]

[a] National Key Lab of Aerospace Power System and Plasma Technology, Xi'an Jiaotong University, 710049 Xi'an, China
[b] School of Mechanical Engineering, Xi'an Jiaotong University, Xi'an, Shaanxi 710049, China
[c] Arts et Métiers Institute of Technology, CNRS, Université de Lorraine, LEM3-UMR7239, F-57000 Metz, France

A B S T R A C T

A new physics-informed deep homogenization neural network (DHN) framework is proposed to identify the homogenized and local behaviors in periodic heterogeneous microstructures. To achieve this, the displacement field is decomposed into averaged and fluctuating contributions, with the local unit cell solution obtained via neural networks subject to periodic boundary conditions. The periodic microstructures are divided into subdomains representing the fiber and matrix phases, respectively. A key contribution of the proposed method is the marriage of elasticity solution and physics-informed neural network to each phase of the composite, namely, the fiber phase as a mesh-free component whose fluctuating displacements are expanded using a discrete Fourier transform, and the matrix phase using material points with fluctuating displacements handled through fully connected neural network layers. The interfacial continuity conditions are enforced by minimizing the traction and displacement differences at separate material points along the interface. Transfer learning is exploited further to facilitate training new microstructures from pre-trained geometry. This hybrid formulation inherently satisfies stress equilibrium equations within the fiber, while efficiently handling the periodic boundary conditions of hexagonal and square unit cells via a series of trainable sinusoidal functions. The innovative use of distinct neural network architectures enables accurate and efficient predictions of displacement and stress when discontinuities are present in the solution fields across the interface. We validate the proposed DHN with the finite-element predictions for unidirectional composites comprised of elastic fiber significantly stiffer than the matrix, under various volume fractions and loading conditions.

1. Introduction

The response of a composite is largely influenced by the complex microstructural features of constituent phases, including their thermomechanical properties, orientation, distribution, and shape. These factors lead to anisotropic and highly nonlinear behavior at the macroscale, making accurate predictions of the constitutive behavior of composites particularly challenging. To address this issue, micromechanics methods have been developed in order to efficiently predict homogenized behavior using detailed information about the thermomechanical properties and microstructure characteristics of each individual phase.

Broadly, micromechanics theories may be classified into two main categories based on how boundary conditions are implemented, namely, nonperiodic homogenization and periodic homogenization approaches (Chen et al., 2018; Pindera et al., 2009). Early work on nonperiodic homogenization approaches centered on solving Eshelby's inclusion problem (Eshelby, 1957), which involves determining displacement and stress fields by embedding an inclusion within an infinite matrix or by embedding both the inclusion and matrix in an effective medium. These methods simplify the complex microstructure of the composites as a representative volume element (RVE). The most commonly used nonperiodic homogenization methods include the self-consistent scheme (Willis, 1977), the composite cylinders/spheres assemblage (Hashin and Rosen, 1964), the generalized self-consistent model (Christensen and Lo, 1979), and the Mori-Tanaka method (Mori and Tanaka, 1973). A significant limitation of these techniques is that they either disregard the interactions between neighboring phases entirely or consider them only in an averaged manner (Chen et al., 2021; Hessman et al., 2021). In many cases, they cannot adequately describe the local stress field distributions, which are critical for predicting the plastic flow and failure modes, and hence the nonlinear stress–strain response, if not the homogenized moduli (Chen and Pindera, 2020).

* Corresponding author at: National Key Lab of Aerospace Power System and Plasma Technology, Xi'an Jiaotong University, 710049 Xi'an, PR China.
E-mail address: phdapple@xjtu.edu.cn (Z. Yang).

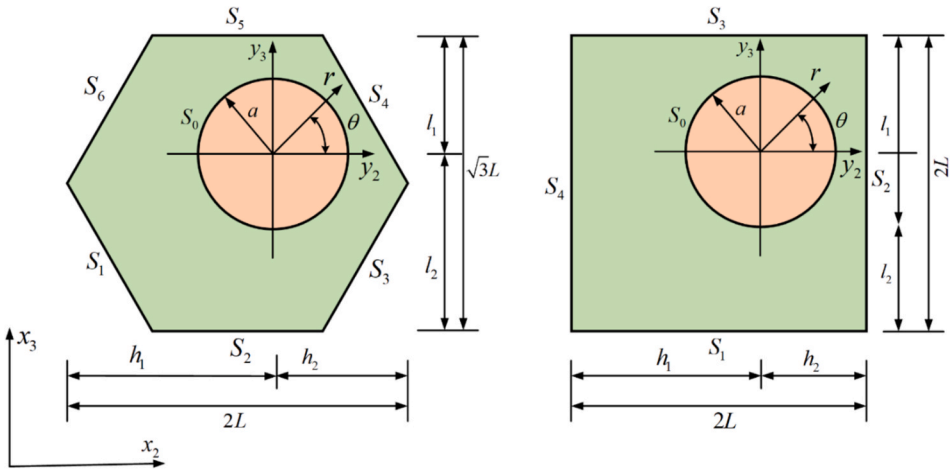

Fig. 1. Hexagonal and square arrays of cylindrical fibers.

Periodic homogenization approaches are based on the assumption that the heterogeneous microstructure is periodically distributed. The behavior of the material-at-large is identical to the homogenized behavior of a repeating unit cell (RUC), namely, the smallest structural unit of the material, replicated in appropriate directions to form the entire material (Pallicity and Böhlke, 2021). The accuracy of the RUC model relies on the accurate satisfaction of displacement and traction periodic boundary conditions on the exterior faces of the RUC. Evidently, the main advantage of the RUC-based approaches is that they explicitly account for the underlying microstructures and their distributions, providing greater accuracy and applicability relative to the RVE-based approaches. Thus far, most RUC-based approaches in the literature have been developed based on the finite-element (Chen et al., 2022; Cruz-González et al., 2020) and finite-volume approaches (Cavalcante and Pindera, 2016; Chen and Pindera, 2020), largely due to the ease with which periodic boundary conditions for displacements can be implemented. However, the conventional finite element method for homogenization has a significant limitation: it is incapable of simultaneously enforcing periodic boundary conditions for tractions. To address this issue, Du et al. (2024) introduced an isogeometric homogenization technique and employed Nitsche's method to correlate the tractions and displacement periodicity conditions. An elasticity-based periodic homogenization theory has been developed by (Drago and Pindera, 2008; He and Pindera, 2021; Wang et al., 2018), referred to as the locally exact homogenization theory (LEHT), where the periodic boundary condition is implemented through a new balanced variational principle.

Over the past few years, there has been a surge of interest in developing surrogate micromechanics models for composite materials through the use of deep learning techniques. For instance, Gajek et al. (2020) proposed a deep material network using a system of interconnected mechanistic building blocks for modelling the nonlinear linear response of short fiber-reinforced composites. Masi and Stefanou (2022) developed the thermodynamics-based artificial neural network for multiscale modeling of inelastic architected materials. Danoun et al. (2024) combined the finite-element method and LSTM recurrent neural networks to solve inelastic multiscale problems. In the abovementioned applications, neural networks with integrated physical constraints are mainly used to derive the homogenized nonlinear stress–strain relation of heterogeneous microstructures. Although they demonstrate strong capabilities in capturing the constitutive behavior of the composites, they only offer an averaged response of the composites but fail to predict the local field variable distributions within the microstructures.

A different class of neural networks has been introduced in the literature (Chen et al., 2025; Henkes et al., 2022; Jiang et al., 2023; Ren and Lyu, 2024; Wu et al., 2023), based on the physics-informed neural networks (PINN) originally developed by Raissi et al. (2019), in an attempt to resolve field variables of interest, such as displacement, stress, and strain fields in heterogeneous microstructures. The PINN approach endows the neural network with the stress equilibrium or the linear momentum equations, as well as the traction and displacement boundary conditions via a collection of material points into the learning process as part of the loss function (Chen et al., 2024; Nguyen-Thanh et al., 2021; Samaniego et al., 2020). The vanilla PINN approach, however, encounters considerable challenges when solving the unit cell problem, particularly in constructing neural network architecture that simultaneously satisfies the stress equilibrium equations, together with accurately enforcing the periodic boundary conditions for displacements and tractions. This difficulty arises because periodicity is typically imposed via a penalty loss term representing the residual norms of the periodic conditions, which can only impose the periodic boundary conditions approximately (Raissi et al., 2019). To address this limitation, several attempts have been made to enforce periodic boundary conditions exactly (Dong and Ni, 2021; Jiang et al., 2023; Linghu et al., 2025; Soyarslan and Pradas, 2024), without relying on explicit constraints between periodically matched boundary collocation points, thereby removing the associated residual loss term. Moreover, PINN struggles with convergence issues when discontinuities are present in the solution fields, which is particularly true in the case of composite materials whose fiber and matrix typically exhibit significant moduli mismatch (Henkes et al., 2022; Linghu et al., 2025).

Herein, for the first time, a novel hybrid deep homogenization neural network (H-DHN) is introduced to predict homogenized moduli and local displacement and stress fields of periodic heterogeneous microstructures. The key contribution of the proposed H-DHN framework is to represent the fluctuating displacements using two novel neural network architectures. Particularly, the fiber phase is treated as a mesh-free component, with the fluctuating displacements expressed by a discrete Fourier transform expansion. This formulation inherently satisfies the stress equilibrium equations in the fiber phase. The unknown coefficients of each harmonic term are determined by minimizing the interface loss terms. In contrast, the matrix phase is characterized by a collection of material (or collocation) points, with the fluctuating displacements represented by fully connected neural network layers. The periodic boundary conditions of hexagonal and square unit cells are precisely enforced using a set of trainable sinusoidal functions. The main advantage of the proposed hybrid network framework lies in its capability to accurately predict the displacement and stress fields within the heterogeneous microstructures wherein significant moduli mismatch exists. Extensive comparison with the finite-element solution of graphite/epoxy and glass/epoxy composites showcases the accuracy of the proposed method.

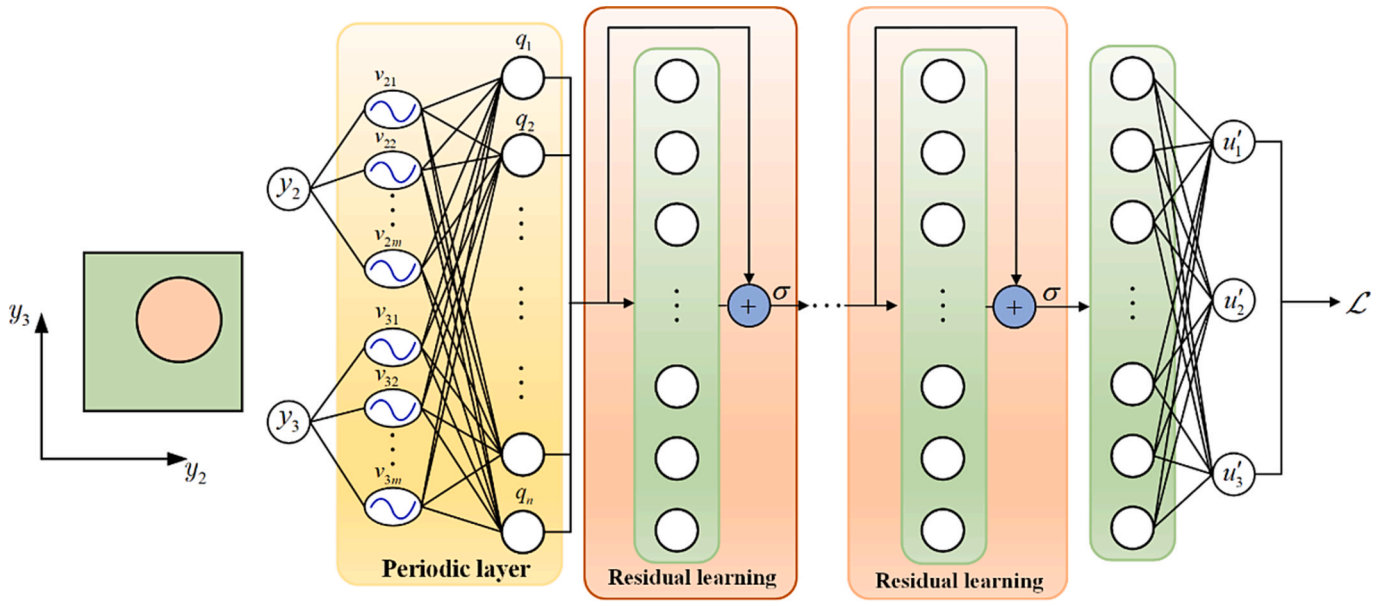

Fig. 2. Physics-informed neural networks acting as surrogate micromechanics model.

2. Theoretical developments

Consider periodic arrays of unidirectional fibers embedded in the matrix phase. The responses of such composites can be characterized by repeating unit cells that define the material's microstructures, subjected to the periodicity boundary conditions, as illustrated in Fig. 1. In the framework of the zeroth-order homogenization theory, the displacement field $u_i^{(q)}$ in each phase of the unit cell can be decomposed into averaged and fluctuating contributions in the global $\boldsymbol{x}$ and local $\boldsymbol{y}$ coordinates, respectively, as follows (Bensoussan et al., 1978; He et al., 2023; He and Pindera, 2020):

$$u_i^{(q)}(\boldsymbol{x},\boldsymbol{y}) = \overline{\varepsilon}_{ij}\cdot x_j + u_i'^{(q)}(\boldsymbol{y}),\ \ i=1,2,3 \tag{1}$$

where $q = f, m$ represent bulk domains occupied by the fiber and matrix, respectively. $\overline{\varepsilon}_{ij}$ indicate the macroscopic (or applied) strains. $u_i'^{(q)}(\boldsymbol{y})$ indicate the fluctuating displacements induced by the microstructures and macroscopic strains $\overline{\varepsilon}_{ij}$. Assuming infinitesimal deformations and rotations, the strains in the qth phase can be obtained as a two-scale expansion using the strain–displacement relation as follows:

$$\varepsilon_{ij}^{(q)} = \overline{\varepsilon}_{ij} + \varepsilon_{ij}'^{(q)} = \overline{\varepsilon}_{ij} + \frac{1}{2}\left(u_{i,j}' + u_{j,i}'\right)^{(q)} \tag{2}$$

For linearly elastic, transversely isotropic bulk phases with the symmetry axis aligned with the principal axis x_1, the constitutive equations read:

$$\boldsymbol{\sigma}^{(q)} = \mathbf{C}^{(q)}\cdot\boldsymbol{\varepsilon}^{(q)} = \boldsymbol{C}^{(q)}\cdot\overline{\boldsymbol{\varepsilon}}^{(q)} + \boldsymbol{C}^{(q)}\cdot\boldsymbol{\varepsilon}'^{(q)} \tag{3}$$

in the above equation, $\boldsymbol{\sigma}^{(q)} = [\sigma_{11},\sigma_{22},\sigma_{33},\sigma_{23},\sigma_{13},\sigma_{12}]^{\mathrm{T}(q)}$, $\boldsymbol{\varepsilon}^{(q)} = [\varepsilon_{11},\varepsilon_{22},\varepsilon_{33},2\varepsilon_{23},2\varepsilon_{13},2\varepsilon_{12}]^{\mathrm{T}(q)}$, $\boldsymbol{C}^{(q)}$ denotes the fourth-order elasticity tensor,

$$\boldsymbol{C}^{(q)} = \begin{bmatrix} E_A + 4k_T\nu_A^2 & 2k_T\nu_A & 2k_T\nu_A & 0 & 0 & 0 \\ 2k_T\nu_A & k_T+\mu_T & k_T-\mu_T & 0 & 0 & 0 \\ 2k_T\nu_A & k_T-\mu_T & k_T+\mu_T & 0 & 0 & 0 \\ 0 & 0 & 0 & \mu_T & 0 & 0 \\ 0 & 0 & 0 & 0 & \mu_A & 0 \\ 0 & 0 & 0 & 0 & 0 & \mu_A \end{bmatrix}^{(q)} \tag{4}$$

where E_A, k_T, μ_T, μ_A and ν_A are the five independent material properties for the transversely isotropic materials, namely, the longitudinal Young's modulus, plane strain bulk modulus, in-plane shear and anti-plane shear moduli, and anti-plane Poisson's ratio, respectively.

In this manuscript, the fluctuating displacements, strains, stresses, and equilibrium equations are formulated in the Cartesian coordinate (y_2, y_3) system for the matrix phase and in the cylindrical coordinate system (r,θ) for the fiber phase of the unit cell. The central idea of the proposed H-DHN method is to represent the fluctuating displacements using two neural network models as follows:

$$\begin{aligned} \left[u_z', u_r', u_\theta'\right]^{(f)} &= \mathcal{NN}^{(f)}[r,\theta], \\ \left[u_1', u_2', u_3'\right]^{(m)} &= \mathcal{NN}^{(m)}[y_2, y_3] \end{aligned} \tag{5}$$

These fluctuating displacements in each subdomain are solved using two distinct approaches. Particularly, the fiber phase is treated as a mesh-free component, with the fluctuating displacements approximated by a discrete Fourier transform expansion. Conversely, the matrix phase is characterized by a collection of material (or collocation) points, with the fluctuating displacements represented by fully connected neural network layers. These displacements are determined strictly under periodic boundary conditions, combined with interfacial continuity conditions.

2.1. Fiber displacements

In the absence of inertia forces, the stress equilibrium conditions expressed in terms of cylindrical coordinate fluctuating displacements u_z', u_r', and u_θ' (with the superscript f omitted for simplicity) read:

$$\begin{aligned} &\frac{\partial^2 u_z'}{\partial r^2} + \frac{1}{r}\frac{\partial u_z'}{\partial r} + \frac{1}{r^2}\frac{\partial^2 u_z'}{\partial \theta^2} = 0 \\ &(k_T+\mu_T)\left(\frac{\partial^2 u_r'}{\partial r^2} + \frac{1}{r}\frac{\partial u_r'}{\partial r} - \frac{u_r'}{r^2}\right) + \frac{\mu_T}{r^2}\frac{\partial^2 u_r'}{\partial \theta^2} + \frac{k_T}{r}\frac{\partial^2 u_\theta'}{\partial r\partial\theta} - \frac{(k_T+2\mu_T)}{r^2}\frac{\partial u_\theta'}{\partial\theta} = 0 \\ &\mu_T\left(\frac{\partial^2 u_\theta'}{\partial r^2} + \frac{1}{r}\frac{\partial u_\theta'}{\partial r} - \frac{\widetilde{u}_\theta}{r^2}\right) + \frac{(k_T+\mu_T)}{r^2}\frac{\partial^2 u_\theta'}{\partial\theta^2} + \frac{k_T}{r}\frac{\partial^2 u_r'}{\partial r\partial\theta} + \frac{(k_T+2\mu_T)}{r^2}\frac{\partial u_r'}{\partial\theta} = 0 \end{aligned} \tag{6}$$

In the fiber phase, the solutions to the fluctuating displacements u_z', u_r', and u_θ' can be represented by a finite sum of harmonic terms using a Fourier expansion in cylindrical coordinates, as follows (Wang et al.,

2018; Wang and Pindera, 2016):

$$
\begin{aligned}
u_z'(r,\theta) &= H_{01} + \sum_{n=1}^{\infty} a(\zeta^n H_{n1}\cos n\theta + \zeta^n H_{n2}\sin n\theta)\\
u_r'(r,\theta) &= F_{01}a\zeta + F_{12}\cos\theta + G_{12}\sin\theta + \sum_{n=2}^{\infty}\sum_{j=1}^{2} a\zeta^{p_{nj}}\left(F_{nj}\cos n\theta + G_{nj}\sin n\theta\right)\\
u_\theta'(r,\theta) &= -F_{12}\sin\theta + G_{12}\cos\theta + \sum_{n=2}^{\infty}\sum_{j=1}^{2} a\beta_{nj}\zeta^{p_{nj}}\left(F_{nj}\sin n\theta - G_{nj}\cos n\theta\right)
\end{aligned}
\tag{7}
$$

where H_{nj},F_{nj} and $G_{nj}(j=1,2)$ are the adjustable neural network training parameters. $\zeta = r/a$ represents the normalized radial coordinate, a is the radius of the fiber. $p_{n1} = n+1, p_{n2} = n-1$ are the two eigenvalues, and

$$
\beta_{nj} = \frac{(k_T+\mu_T)\left(1-p_{nj}^2\right)+\mu_T n^2}{n\left(k_T p_{nj} - k_T - 2\mu_T\right)}
\tag{8}
$$

The strains $\boldsymbol{\varepsilon} = [\varepsilon_{zz}, \varepsilon_{rr}, \varepsilon_{\theta\theta}, 2\varepsilon_{r\theta}, 2\varepsilon_{zr}, 2\varepsilon_{z\theta}]^{\mathrm{T}}$ in the cylindrical coordinates are computed using automatic differentiation in the PyTorch library:

$$
\begin{aligned}
\varepsilon_{zz} &= \bar{\varepsilon}_{zz} + \frac{\partial u_z'}{\partial z}\\
\varepsilon_{rr} &= \bar{\varepsilon}_{rr} + \frac{\partial u_r'}{\partial r}\\
\varepsilon_{\theta\theta} &= \bar{\varepsilon}_{\theta\theta} + \frac{u_r'}{r} + \frac{1}{r}\frac{\partial u_\theta'}{\partial \theta}\\
\varepsilon_{r\theta} &= \bar{\varepsilon}_{r\theta} + \frac{1}{2}\left(\frac{1}{r}\frac{\partial u_r'}{\partial \theta} + \frac{\partial u_\theta'}{\partial r} - \frac{u_\theta'}{r}\right)\\
\varepsilon_{rz} &= \bar{\varepsilon}_{rz} + \frac{1}{2}\frac{\partial u_z'}{\partial r}\\
\varepsilon_{\theta z} &= \bar{\varepsilon}_{\theta z} + \frac{1}{2r}\frac{\partial u_z'}{\partial \theta}
\end{aligned}
\tag{9}
$$

Using Hooke's law, the stresses $\boldsymbol{\sigma} = [\sigma_{zz}, \sigma_{rr}, \sigma_{\theta\theta}, \sigma_{r\theta}, \sigma_{zr}, \sigma_{z\theta}]^{\mathrm{T}}$ in the cylindrical coordinates are obtained as follows:

$$
\boldsymbol{\sigma} = \boldsymbol{C\varepsilon}
\tag{10}
$$

2.2. Matrix displacements

As shown in Fig. 2, a deep neural network with several residual layers is employed to approximate the fluctuating displacements u_1', u_2', u_3' in the matrix phase. The inputs q_j^{l-1} and outputs q_j^l of the lth layer are propagated through the network as follows:

$$
q_j^l = \sigma\left(w_{i,j}^l q_i^{l-1} + b_j^l + q_i^{l-1}\right)
\tag{11}
$$

In the equation above, $w_{i,j}^l$ and b_j^l denote the weights and biases of the lth layer, respectively. σ indicates the nonlinear activation function.

To ensure the exact satisfaction of the periodicity characteristics of the RUC, the neural network architecture is modified by incorporating a set of sinusoidal functions (Dong and Ni, 2021). Towards this end, the spatial coordinates (y_2, y_3) are transformed to:

$$
\left(\frac{2\pi}{d_2}y_2, \frac{2\pi}{d_3}y_3\right) \rightarrow (y_2', y_3')
\tag{12}
$$

for square arrays of fibers, d_2 and d_3 define the periods of the unit cell in pertinent directions, and

$$
\left(\frac{4\pi}{\sqrt{3}L}y_2, \frac{2\pi}{\sqrt{3}L}y_2 + \frac{2\pi}{L}y_3\right) \rightarrow (y_2', y_3')
\tag{13}
$$

for hexagonal arrays of fibers, L denotes the width of each side of the hexagon. The modified coordinates, which are mapped through a number of harmonic functions with specified periods and tunable parameters (Dong and Ni, 2021), ensure that the neural network's outputs precisely satisfy the periodicity conditions to any desired degree:

$$
\begin{aligned}
v_{2i}(y_2) &= \sigma\left[A_{2i}\cos\left(y_2' + \phi_{2i}\right) + c_{2i}\right],\\
v_{3i}(y_3) &= \sigma\left[A_{3i}\cos\left(y_3' + \phi_{3i}\right) + c_{3i}\right],\\
q_j(y_2, y_3) &= \sigma\left[\sum_{i=1}^{m} v_{2i}(y_2) W_{ij}^{(2)} + \sum_{i=1}^{m} v_{3i}(y_3) W_{ij}^{(3)} + B_j\right]
\end{aligned}
\tag{14}
$$

In the above equation,$1 \leqslant i \leqslant m$ and $1 \leqslant j \leqslant n$. A_{2i}, A_{3i}, ϕ_{2i}, ϕ_{3i}, c_{2i}, c_{3i}, $W_{ij}^{(2)}$, $W_{ij}^{(3)}$ and B_j indicate the adjustable parameters trained by the neural networks. As before, the matrix strains in the Cartesian coordinates (in Eq. (2)) are evaluated directly using automatic differentiation, while the matrix stresses are determined using Hooke's law in Eq. (3).

In the matrix phase, the equilibrium equations expressed in terms of u_1', u_2', u_3' in the Cartesian coordinates read:

$$
\begin{aligned}
\mathscr{L}_1 &= \frac{\partial^2 u_1'}{\partial y_2^2} + \frac{\partial^2 u_1'}{\partial y_3^2} = 0\\
\mathscr{L}_2 &= (k_T+\mu_T)\frac{\partial^2 u_2'}{\partial y_2^2} + \mu_T\frac{\partial^2 u_2'}{\partial y_3^2} + k_T\frac{\partial^2 u_3'}{\partial y_2 \partial y_3} = 0\\
\mathscr{L}_3 &= k_T\frac{\partial^2 u_2'}{\partial y_2 \partial y_3} + \mu_T\frac{\partial^2 u_3'}{\partial y_3^2} + (k_T+\mu_T)\frac{\partial^2 u_3'}{\partial y_2 \partial y_3} = 0
\end{aligned}
\tag{15}
$$

2.3. Construction of loss function

The microscopic displacements in the matrix $\left[u_1', u_2', u_3'\right]$ and the fiber $\left[u_z', u_r', u_\theta'\right]$ phases are obtained by minimizing a common loss function, which incorporates the residuals of the PDEs in the matrix phase, as well as the displacements and tractions continuity conditions at the interfaces:

$$
\mathscr{L} = \mathscr{L}_{PDE} + \mathscr{L}_{Con}
\tag{16}
$$

where

$$
\mathscr{L}_{PDE} = \frac{1}{N_b}\sum_{e=1}^{N_b} \lambda_{PDE}^e \left[\mathscr{L}_1^2 + \mathscr{L}_2^2 + \mathscr{L}_3^2\right]\big|_{(y_2^e, y_3^e)}
\tag{17}
$$

$$
\mathscr{L}_{Con} = \frac{1}{N_i}\sum_{e=1}^{N_i} \lambda_{Con}^e \left[[\![t_1]\!]^2 + [\![t_2]\!]^2 + [\![t_3]\!]^2 + [\![u_1']\!]^2 + [\![u_2']\!]^2 + [\![u_3']\!]^2\right]\big|_{(y_2^e, y_3^e)}
\tag{18}
$$

where N_b and N_i represent the number of collocation points within the matrix materials and on the fiber/matrix interface, respectively. $t_i = \sigma_{ij} n_j$ from the Cauchy relation, n_j denotes the component of the unit normal vector. $[\![\{\cdot\}]\!] = \{\cdot\}^+ - \{\cdot\}^-$ captures the difference in displacements and tractions between the matrix and fiber sides of the interface in the Cartesian coordinates. λ_{PDE}^e and λ_{Con}^e are adjustable weights assigned to each collocation point.

Eventually, to obtain solutions for the fluctuating displacements under given macroscopic strains, we minimize the overall loss $\mathscr{L}$ with respect to the network parameters $\boldsymbol{\theta}$ by applying gradient descent. Concurrently, we seek to maximize the total loss function $\mathscr{L}$ respective to the adaptive weights λ_{PDE}^e and λ_{Con}^e using gradient ascent as follows (McClenny and Braga-Neto, 2023):

$$
\begin{aligned}
\boldsymbol{\theta}^{k+1} &= \boldsymbol{\theta}^k - \eta_k \nabla_{\boldsymbol{\theta}} \mathscr{L} \ominus,\\
\lambda_{PDE}^{k+1} &= \lambda_{PDE}^k + \rho_{PDE}^k \nabla_{\lambda PDE} \mathscr{L} \ominus, \ominus\\
\lambda_{Con}^{k+1} &= \lambda_{Con}^k + \rho_{Con}^k \nabla_{\lambda_{Con}} \mathscr{L} \ominus
\end{aligned}
\tag{19}
$$

where $\boldsymbol{\theta} = \left\{H_{nj}, F_{nj}, G_{nj}, A_{2i}, A_{3i}, \phi_{2i}, \phi_{3i}, c_{2i}, c_{3i}, W_{ij}^{(2)}, W_{ij}^{(3)}, B_j, w_{i,j}^l, b_j^l\right\}$, η_k represents the gradually decreasing learning rate for the network parameters $\boldsymbol{\theta}$ at the kth step. $\rho_{(\cdot)}^k$ is a distinct learning rate associated with

Table 1

Elastic fiber and matrix properties employed in the calculations.

Materials	E_A(GPa)	E_T(GPa)	μ_A(GPa)	μ_T(GPa)	ν_A
AS4 carbon fiber	225	15	15	7	0.2
Glass fiber	72.4	72.4	29.67	29.67	0.22
Epoxy matrix	4.2	4.2	1.567	1.567	0.34

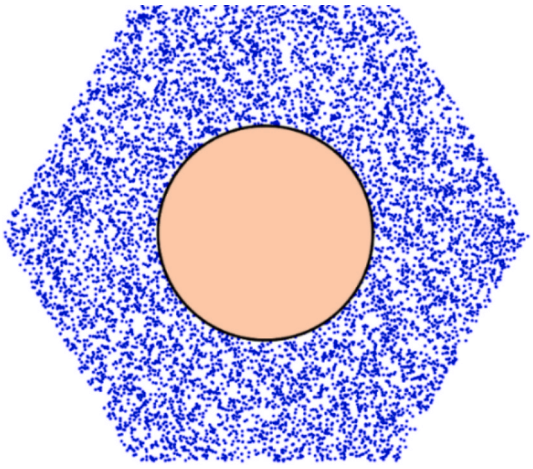

Fig. 3. Collocation point distribution in hexagonal unit cell with 20% volume fraction.

the adaptive weights. It is worth noting that this adaptive weight training technique automatically assigns higher weight to material or collocation points that are more difficult to learn, providing an important advantage over the nonadaptive loss weight parameters (McClenny and Braga-Neto, 2023; Wu et al., 2024).

3. Numerical results

3.1. Local field variables

In this section, we verify the predictive capabilities of the H-DHN theory to accurately generate the homogenized moduli and local stress field of graphite or carbon fiber-reinforced plastics (CFRP) and glass fiber-reinforced plastics (GFRP) composites with two large fiber/matrix modulus contrasts. The material's elastic moduli of each phase are given in Table 1. Specifically, the AS4 graphite fiber exhibits transverse isotropy, with the in-plane Young's modulus 3.56 times stiffer than that of the epoxy. In contrast, the glass fiber is isotropic, with Young's modulus 17.2 times higher than that of the epoxy.

First, we investigate the effect of the neural network depth and number of neurons on inferring the unit cell's fluctuating displacements. As shown in Fig. 3, we consider a hexagonal array of AS4 fiber in the epoxy matrix. The fiber volume fraction is prescribed as 20 %. The unit cell is subjected to a uniaxial transverse strain of $\bar{\varepsilon}_{22} = 1\%$, as is the most demanding. For the matrix phase, we employ four neural network architectures, namely, network 1: $[2-20-20-20-2]$, network 2: $[2-30-30-30-30-2]$, network 3: $[2-40-40-40-40-40-2]$, network 4: $[2-50-50-50-50-50-50-2]$. For the fiber phase, we use 8 harmonic terms in the Fourier expansion representation of fiber fluctuating displacements. The number of collocation points for the two loss terms in Eq. (16) are $N_b = 8000$ and $N_i = 360$. Note that the points of N_b are randomly distributed within the bulk matrix while the points of N_i are uniformly distributed along the fiber/matrix interface. The H-DHN model was trained using Adam Optimizer for 20 k epochs with decreasing learning rates of 1×10^{-2}, 5×10^{-3}, 2.5×10^{-3} and 1.25×10^{-3} (5 k epochs for each). Notice that the learning rate for adaptive weights was held at 5×10^{-3} after 10 k iterations. We use the rectifier (ReLU) function as the default activation function.

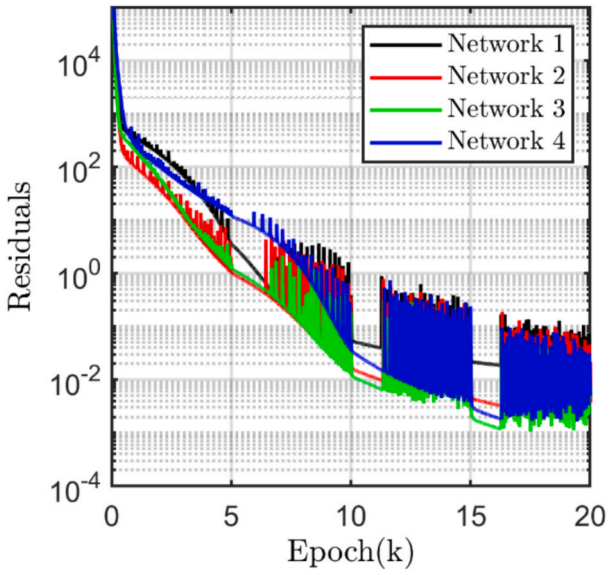

Fig. 4. Effect of neural network depth and number of neurons on the training loss function.

Fig. 4 compares the evolution of the loss function for the four neural networks that we study. We observe that neural networks 2 and 3 generate the lowest loss after 10 k training epochs, indicating superior performance at given epochs. Fig. 5 shows the comparison of inferred fluctuating displacement u_2' distributions. We find that the four selected neural networks predict virtually identical results for the fluctuating displacement u_2'.

We further examine the impact of the harmonic terms for the fiber phase on the inferred unit cell solutions, utilizing network 2 for the matrix due to its high accuracy. We focus on four harmonic terms, namely, $n = 2, 5, 8, 12$. The convergence of loss functions for the four harmonic terms is displayed in Fig. 6. We find that $n = 5$ yields the lowest loss, while a higher harmonic number produces a slightly increased loss. We attribute this to the fact that higher-order harmonic terms are typically small, making the stabilization of their coefficients prone to causing fluctuations in the loss function. In Fig. 7, we illustrate the comparison of inferred fluctuating displacement u_2' distributions for different harmonic terms. We observe that the networks with different harmonic terms predict almost the same fluctuating displacement distributions. In Fig. 8, we show the differences between network and FEM predictions of fluctuating displacements. The results indicate that the differences between the two methods are negligible for $n = 5, 8, 12$. The prediction using two harmonic terms $n = 2$ is less favorable in the vicinity of the fiber/matrix interface as $n = 2$ may be inadequate to capture the high-stress gradients in this region. However, the primary features of the displacement and stress distributions are still well predicted with good accuracy.

Fig. 9 shows the transverse normal σ_{22}, σ_{33} and transverse shear σ_{23} stress distributions generated by networks with $n = 2$ and $n = 8$ harmonic terms and FEM techniques. No discernible differences are observed even with only 2 harmonic terms. Comparison of the absolute errors between the neural network and FEM predictions is presented in Fig. 10. We note that differences between the DHN and FEM are further reduced when 8 harmonic terms are used.

To further assess the accuracy of the proposed H-DHN theory, we use network 2 with 8 harmonic terms to predict the local displacements and stresses under various loading conditions. To highlight the effect of adjacent fiber interaction, we subject a hexagonal unit cell with 50 % fiber volume content to a uniaxial transverse strain of $\bar{\varepsilon}_{23} = 1\%$. The number of residual points for the two loss terms in Eq. (16) are $N_b =$

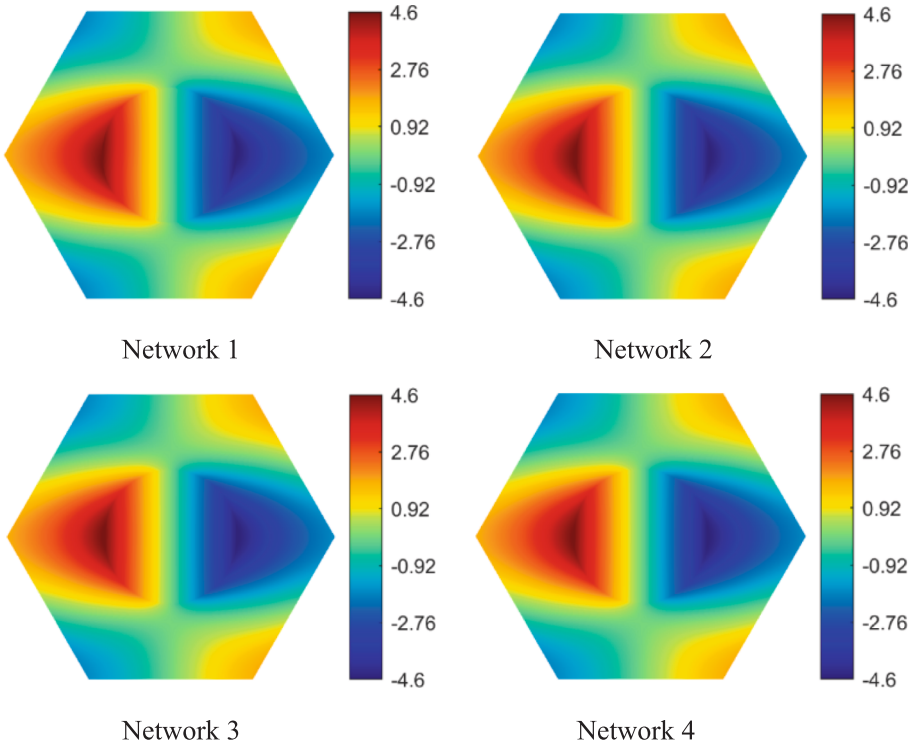

Fig. 5. Comparison of the fluctuating displacement u_2' distributions generated with different network architectures at the uniaxial macroscopic transverse strain of $\bar{\varepsilon}_{22} = 1\%$.

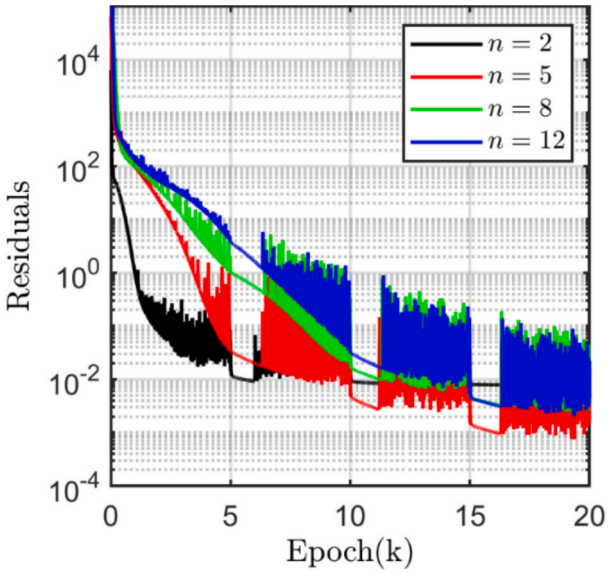

Fig. 6. Effect of harmonic terms in the fiber phase on the training loss function

5000 and $N_i = 360$. Fig. 11 compares the fluctuating displacement u_2' and u_3' distributions generated with the H-DHN and FEM approaches. Fig. 12 illustrates the corresponding results for transverse normal σ_{22}, σ_{33} and shear σ_{23} stresses. Comparable results are obtained throughout the matrix and fiber phases, providing additional support for the proposed H-DHN method.

In the last case of example, we consider square unit cell reinforced with glass fiber. As before, the fiber volume fraction is 50 %. We use $N_b = 5000$ and $N_i = 360$ residual points for the two loss terms in Eq. (16). We apply anti-plane shear strain of $\bar{\varepsilon}_{12} = 1\%$. Fig. 13 presents the distribution of axial shear stresses σ_{12} and σ_{13}. As anticipated, comparison with FEM results is highly favorable.

3.2. Homogenized moduli

In Fig. 14, we compare three of five homogenized engineering moduli of hexagonal arrays of CFRP and GFRP composites as a function of fiber volume fractions in the range of $V_f \in [0.05, 0.65]$ using the H-DHN theory with FEM predictions. Note that the effective transverse Young's moduli E_T^* and axial shear moduli G_A^* have been normalized by the corresponding matrix values, whereas the transverse Poisson's ratios ν_T^* have not been normalized. It is observed that the proposed H-DHN theory correlates very well with the FEM for the two material systems over the entire volume fraction ranges. Effective transverse Young's moduli E_T^* and axial shear moduli G_A^* progressively approach the fiber values as the volume fraction increases. The transverse Poisson's ratios ν_T^* initially increase and then decrease toward the fiber values, as a result of load redistributions.

3.3. Transfer learning H-DHN

Having demonstrated the accuracy of the proposed H-DHN method, we explore the applicability of applying transfer learning to enhance the efficiency of the proposed framework. The key concept is to employ the trained parameters of an existing neural network in a previous example to efficiently train new neural network models for unseen microstructures. This approach is motivated by the observation that variations in geometries, following the same loading direction, do not significantly alter the fundamental characters of stress distributions within the unit cell.

Toward this end, we apply the pre-trained model from Network 2 in Fig. 5, which was originally trained on a hexagonal microstructure with 20 % fiber content, to a square microstructure with 25 % volume fraction. Furthermore, the fiber's position was shifted from the origin to the new coordinates (0.266, 0.266). It should be noted that to eliminate significant updates of the pre-trained parameters, we employ smaller

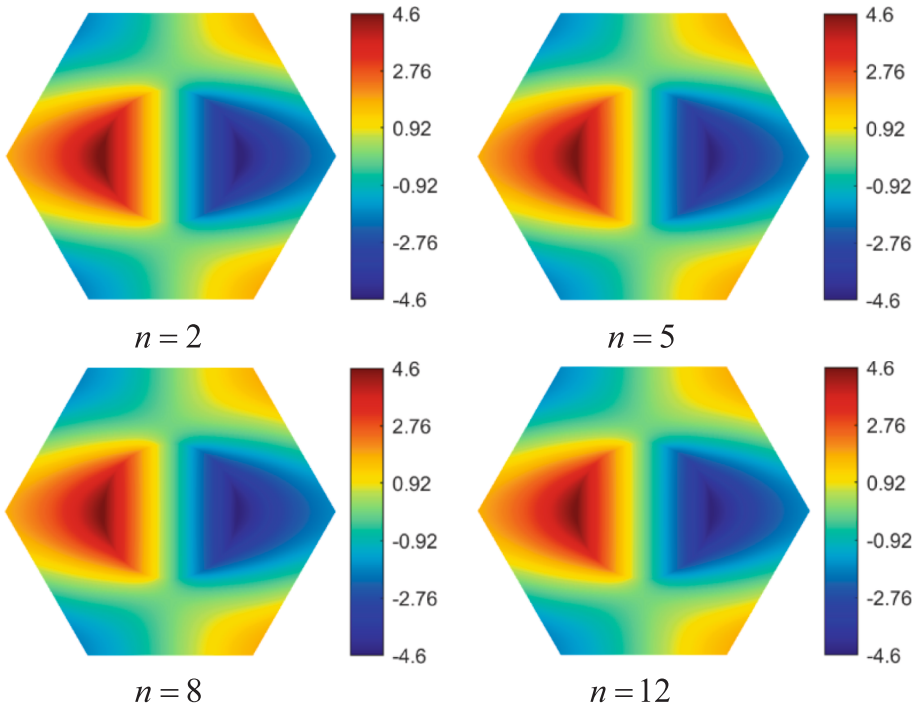

Fig. 7. Comparison of the fluctuating displacement u_2' distributions generated with H-DHN using different harmonic terms at the uniaxial macroscopic transverse strain of $\bar{\varepsilon}_{22} = 1\%$.

learning rates of 1×10^{-3}, 5×10^{-4}, 2.5×10^{-4} and 1.25×10^{-4}(2.5 k epochs for each) for the transfer learning model. Fig. 15 illustrates the variation of the loss functions for both the transfer learning model and the direct training model (where the network was initialized randomly at the first epoch). We find that the transfer learning model converges much faster, with its loss value at any given epoch being significantly lower than that of the direct training model. Fig. 16 presents comparison of the in-plane stress components σ_{22}, σ_{33} and σ_{23} generated with the transfer learning scheme, direct training model, and FEM approach. The results clearly demonstrate a remarkable correlation between the transfer learning model and finite-element benchmark results, whereas the direct training model requires significantly more training epochs to achieve comparable accuracy.

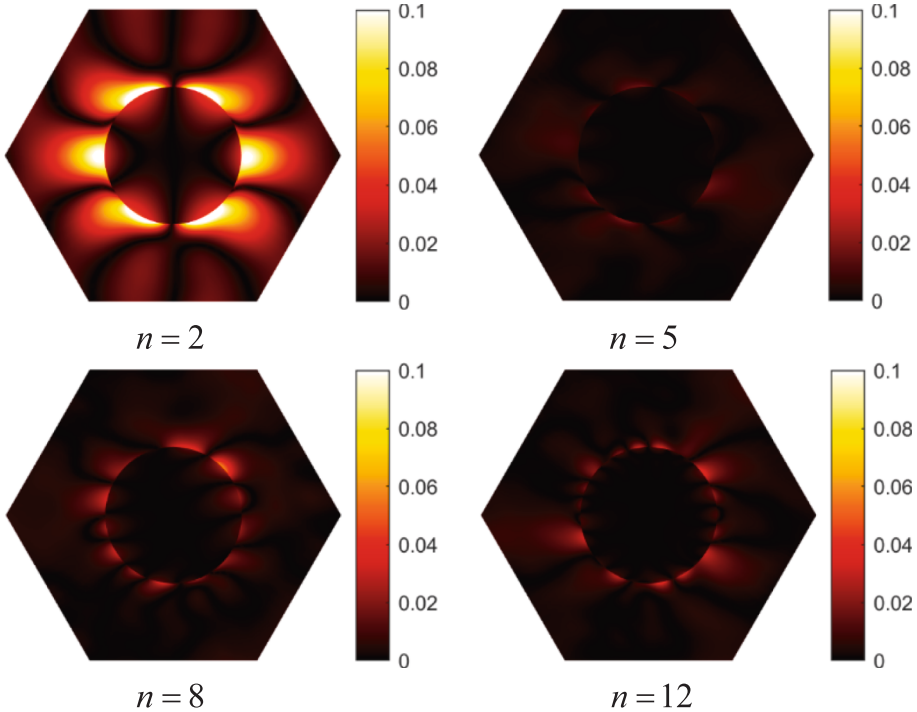

Fig. 8. Comparison of the absolute differences in fluctuating displacement u_2' distributions generated with H-DHN using different harmonic terms and FEM at the uniaxial macroscopic transverse strain of $\bar{\varepsilon}_{22} = 1\%$.

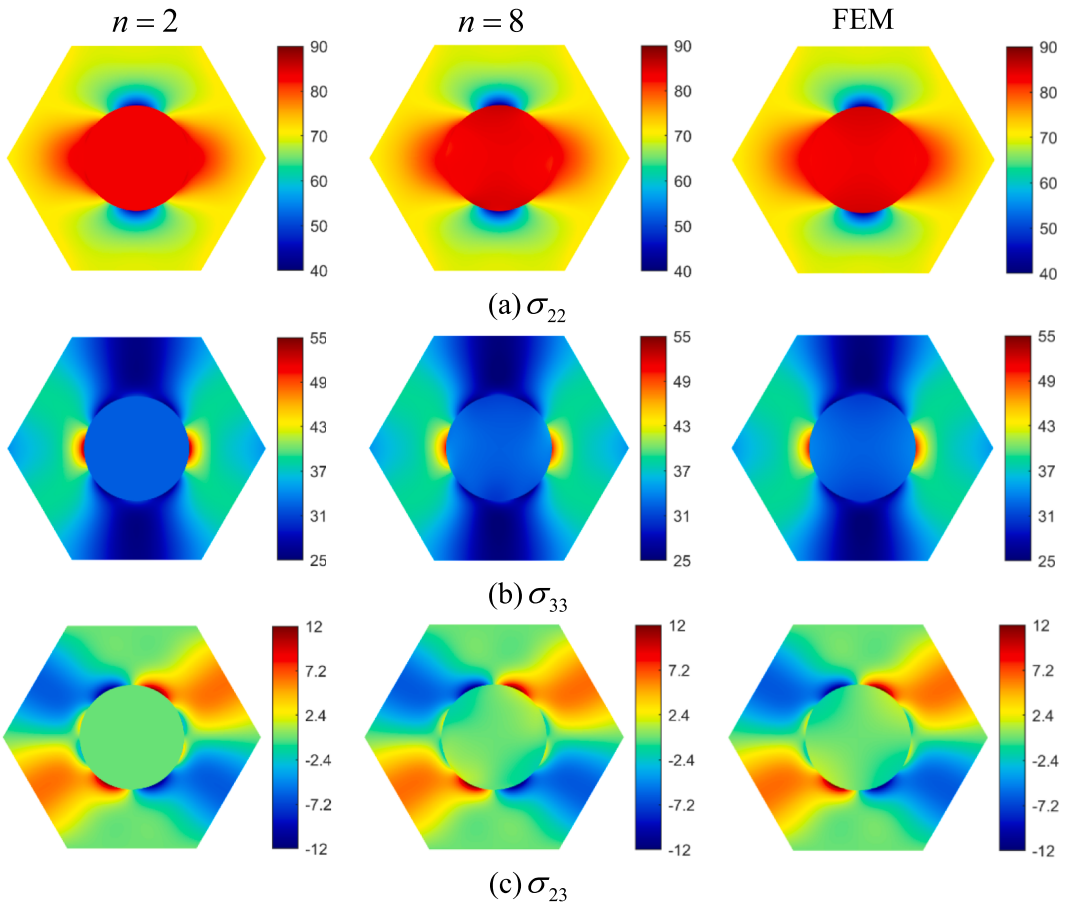

Fig. 9. Comparison of transverse normal σ_{22}, σ_{33} and shear stress σ_{23} distributions generated with H-DHN and the FEM at the uniaxial macroscopic transverse strain of $\bar{\varepsilon}_{22} = 1\%$.

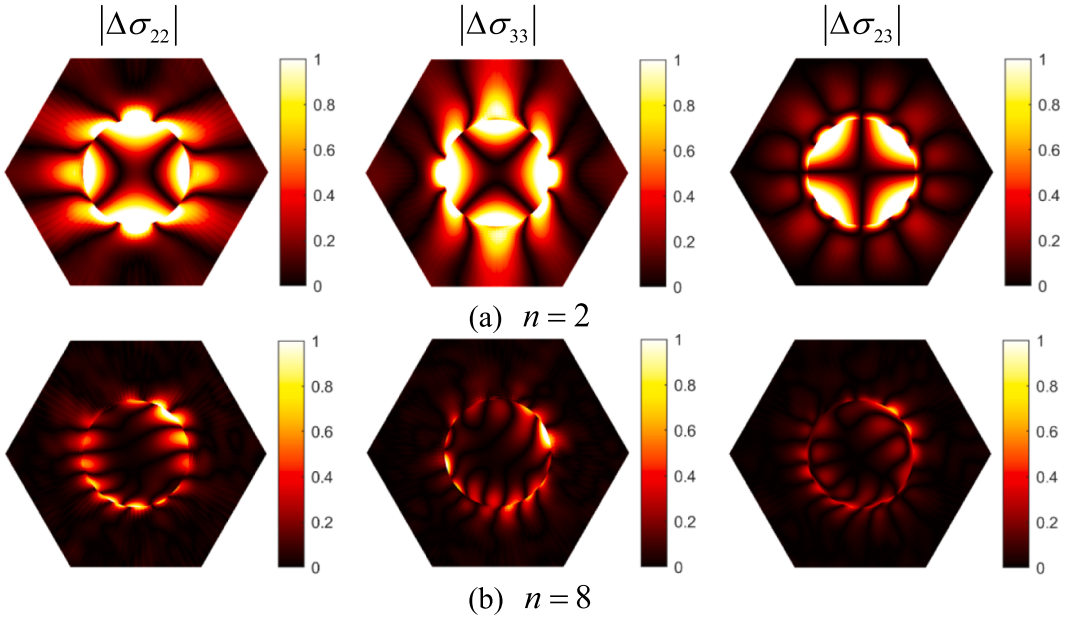

Fig. 10. Comparison of the absolute differences in predicted transverse normal σ_{22}, σ_{33} and shear stress σ_{23} distributions generated with H-DHN using 2 and 8 harmonic terms and FEM at the uniaxial macroscopic transverse strain of $\bar{\varepsilon}_{22} = 1\%$.

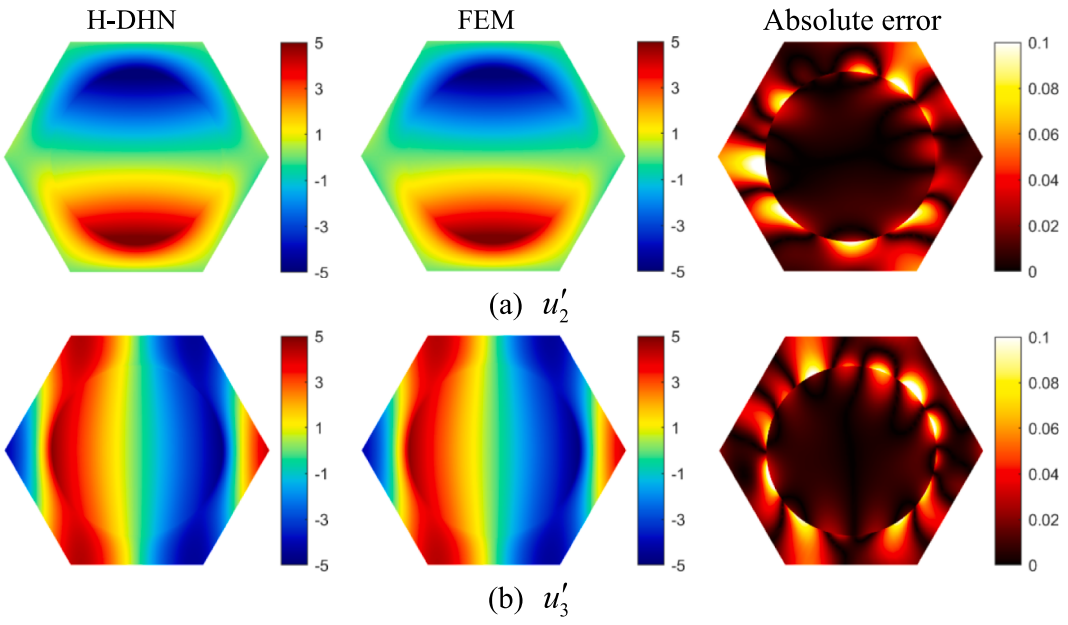

Fig. 11. Comparison of fluctuating displacements u_2' and u_3' generated with H-DHN and FEM at the uniaxial macroscopic transverse shear strain of $\bar{\varepsilon}_{23} = 1\%$.

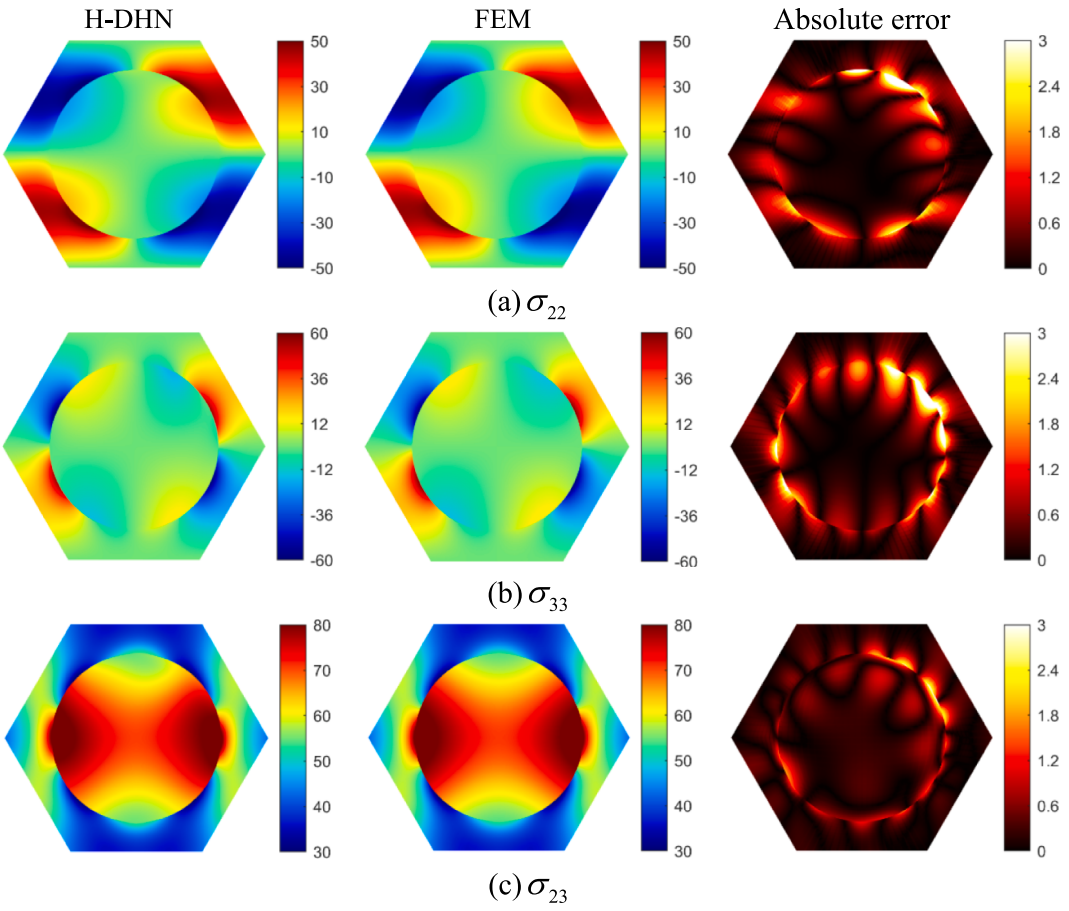

Fig. 12. Comparison of transverse normal σ_{22}, σ_{33} and shear stress σ_{23} distributions generated with H-DHN and FEM at the uniaxial macroscopic transverse shear strain of $\bar{\varepsilon}_{23} = 1\%$.

4. Conclusions

This work presents a new physically informed deep learning framework aimed to accurately predicting homogenized and local responses in periodic heterogeneous microstructures. The periodic microstructures are first divided into subdomains representing each phase of the composite. The proposed approach then uses the discrete Fourier transform along with fully connected neural networks to solve stress equilibrium governing partial differential equations for the fiber and matrix phases, respectively. The two neural networks are seemingly connected via a

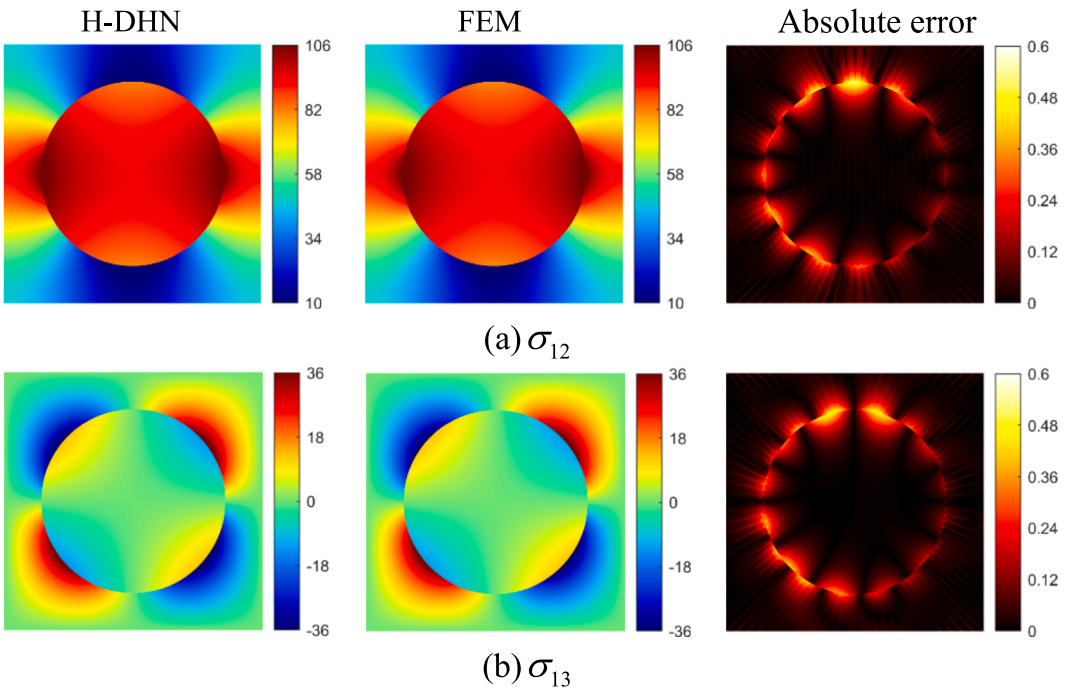

Fig. 13. Comparison of axial shear stress σ_{12} and σ_{13} distributions generated with H-DHN and FEM at the uniaxial macroscopic transverse shear strain of $\bar{\varepsilon}_{12} = 1\%$.

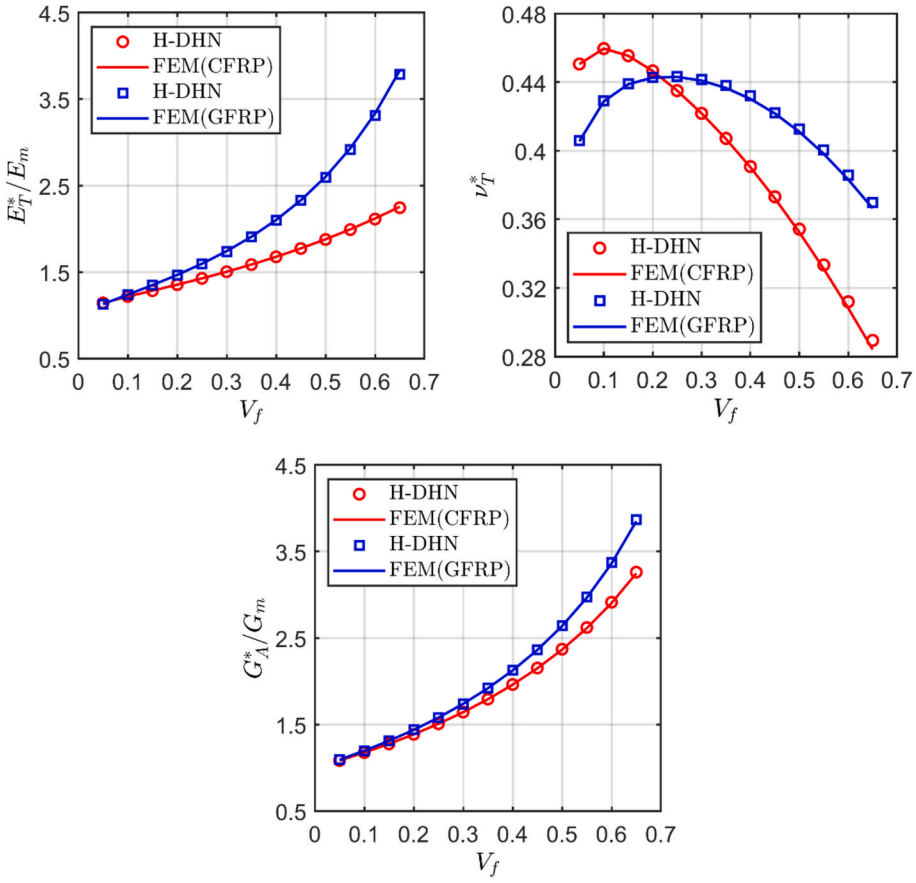

Fig. 14. Comparison of homogenized moduli of hexagonal arrays of CFPR and GFRP composites generated with the H-DHN and FEM.

loss function representing the interfacial traction and displacement continuity conditions. The developed hybrid homogenization method offers several key advantages over the vanilla PINN approach. It exactly satisfies stress equilibrium within the fiber domain, is particularly effective for solving fields with discontinuities due to the fiber/matrix moduli mismatch, and ensures exact compliance with periodicity

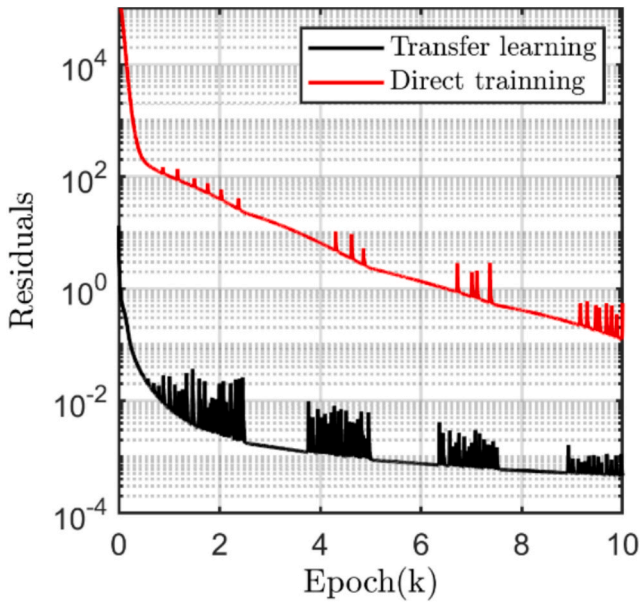

Fig. 15. Comparison of transfer learning and direct training loss values as a function of training epoch.

boundary conditions. The effectiveness of the H-DHN model was demonstrated upon extensive comparison of local field distributions and homogenized moduli for graphite/epoxy and glass/epoxy composite systems with the finite-element unit cell solutions with a wide variety of volume fractions and loading directions. We find that the displacement and stress field in the fiber phase can be represented with sufficient accuracy using as few as two harmonic terms. We also demonstrate the potential of using transfer learning techniques to accelerate the training of unseen microstructures by leveraging an existing neural network model for known geometry.

CRediT authorship contribution statement

Qiang Chen: Writing – original draft, Validation, Supervision, Methodology, Investigation, Formal analysis, Conceptualization. **Wenhui Zhao:** Writing – review & editing, Visualization, Methodology, Investigation, Formal analysis. **Ce Xiao:** Writing – review & editing, Validation, Methodology, Investigation, Formal analysis, Conceptualization. **Zhibo Yang:** Writing – review & editing, Validation, Methodology, Investigation, Formal analysis, Conceptualization. **George Chatzigeorgiou:** Writing – review & editing, Validation, Methodology, Investigation, Formal analysis, Conceptualization. **Fodil Meraghni:** Writing – review & editing, Methodology, Investigation, Formal analysis. **Xuefeng Chen:** Writing – review & editing, Validation, Methodology, Investigation, Funding acquisition, Formal analysis.

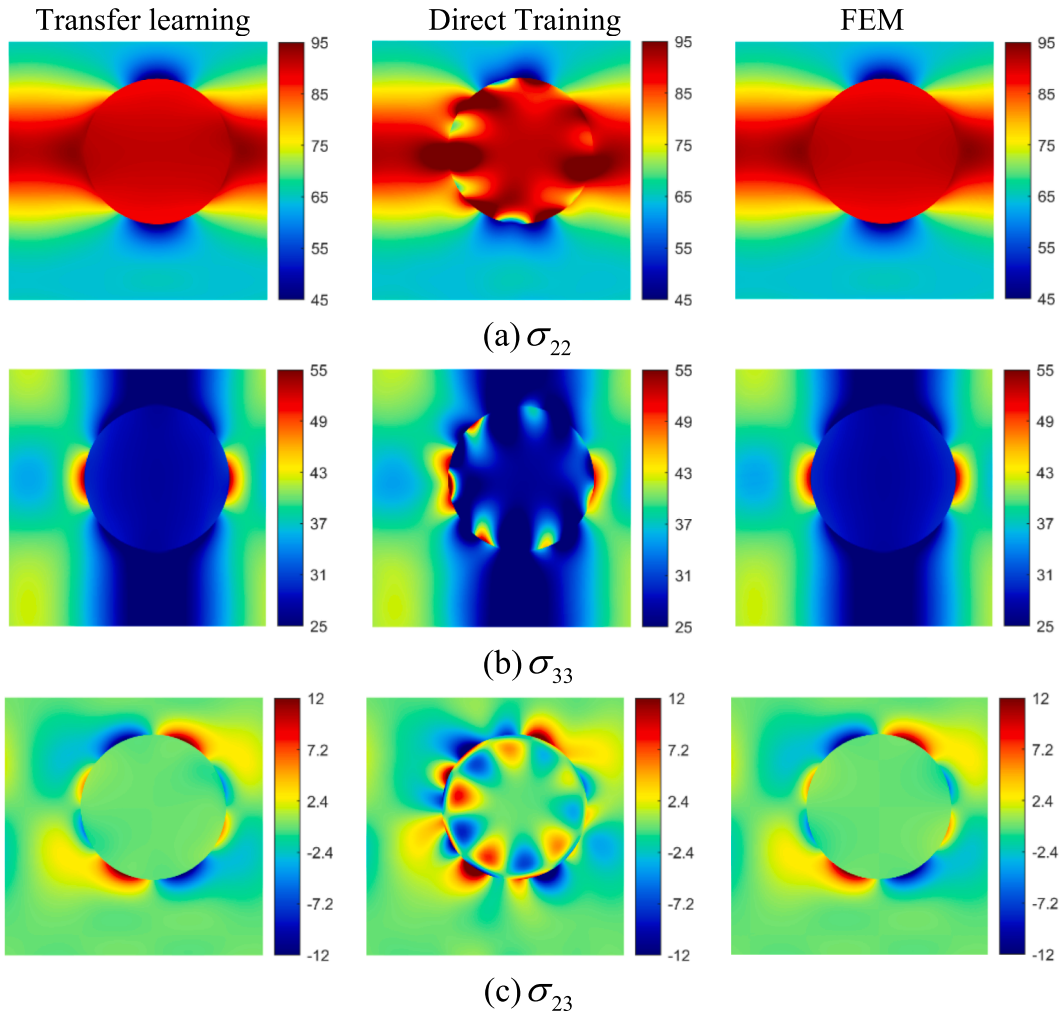

Fig. 16. Comparison of transverse normal σ_{22}, σ_{33} and shear stress σ_{23} distributions generated with transfer learning, direct H-DHN and FEM at the uniaxial macroscopic transverse shear strain of $\bar{\varepsilon}_{22} = 1\%$.

Declaration of competing interest

The authors declare that they have no known competing financial interests or personal relationships that could have appeared to influence the work reported in this paper.

Acknowledgment

Qiang Chen acknowledges the financial support of the National Natural Science Foundation of China (Grant No. 52505126) and National Key Research and Development Program of China (Grant No. 2024YFB4609000). Zhibo Yang acknowledges the financial support of the National Natural Science Foundation of China (Grant No. 92360306).

Data availability

Data will be made available on request.

References

Bensoussan, A., Lions, J.-L., Papanicolau, G., 1978. Asymptotic analysis for periodic structures. North Holland, Amsterdam..

Cavalcante, M.A.A., Pindera, M.-J., 2016. Generalized FVDAM theory for elastic–plastic periodic materials. Int. J. Plast 77, 90–117.

Chen, Q., Chatzigeorgiou, G., Meraghni, F., 2021. Extended mean-field homogenization of viscoelastic-viscoplastic polymer composites undergoing hybrid progressive degradation induced by interface debonding and matrix ductile damage. Int. J. Solids Struct. 210–211, 1–17.

Chen, Q., Chatzigeorgiou, G., Meraghni, F., Javili, A., 2022. Homogenization of size-dependent multiphysics behavior of nanostructured piezoelectric composites with energetic surfaces. European Journal of Mechanics-A/Solids 96, 104731.

Chen, Q., Du, X., Chatzigeorgiou, G., Meraghni, F., Zhao, G., Yang, Z., 2025. Physics-informed deep neural networks towards finite strain homogenization of unidirectional soft composites. Eur. J. Mech. A Solids 114, 105752.

Chen, Q., Pindera, M.-J., 2020. Homogenization and localization of elastic-plastic nanoporous materials with Gurtin-Murdoch interfaces: An assessment of computational approaches. Int. J. Plast 124, 42–70.

Chen, Q., Wang, G., Pindera, M.-J., 2018. Homogenization and localization of nanoporous composites-A critical review and new developments. Compos. B Eng. 155, 329–368.

Chen, Q., Xiao, C., Yang, Z., Tabet, J., Chen, X., 2024. Deep neural network homogenization of multiphysics behavior for periodic piezoelectric composites. Compos. A Appl. Sci. Manuf. 186, 108421.

Christensen, R.M., Lo, K.H., 1979. Solutions for effective shear properties in three phase sphere and cylinder models. J. Mech. Phys. Solids 27, 315–330.

Cruz-González, O.L., Rodríguez-Ramos, R., Otero, J.A., Ramírez-Torres, A., Penta, R., Lebon, F., 2020. On the effective behavior of viscoelastic composites in three dimensions. Int. J. Eng. Sci. 157, 103377.

Danoun, A., Prulière, E., Chemisky, Y., 2024. FE-LSTM: A hybrid approach to accelerate multiscale simulations of architectured materials using Recurrent Neural Networks and Finite Element Analysis. Comput. Methods Appl. Mech. Eng. 429, 117192.

Dong, S., Ni, N., 2021. A method for representing periodic functions and enforcing exactly periodic boundary conditions with deep neural networks. J. Comput. Phys. 435, 110242.

Drago, A.S., Pindera, M.-J., 2008. A Locally Exact Homogenization Theory for Periodic Microstructures With Isotropic Phases. J. Appl. Mech. 75.

Du, X., Chen, Q., Chatzigeorgiou, G., Meraghni, F., Zhao, G., Chen, X., 2024. Nitsche's method enhanced isogeometric homogenization of unidirectional composites with cylindrically orthotropic carbon/graphite fibers. Compos. Sci. Technol. 256, 110787.

Eshelby, J.D., 1957. The determination of the elastic field of an ellipsoidal inclusion, and related problems. Proc. R. Soc. Lond. A 241, 376–396.

Gajek, S., Schneider, M., Böhlke, T., 2020. On the micromechanics of deep material networks. J. Mech. Phys. Solids 142, 103984.

Hashin, Z., Rosen, B.W., 1964. The Elastic Moduli of Fiber-Reinforced Materials. J. Appl. Mech. 31, 223–232.

He, Z., Liu, J., Chen, Q., 2023. Higher-order asymptotic homogenization for piezoelectric composites. Int. J. Solids Struct. 264, 112092.

He, Z., Pindera, M.-J., 2020. Finite Volume-Based Asymptotic Homogenization of Periodic Materials Under In-Plane Loading. J. Appl. Mech. 87.

He, Z., Pindera, M.-J., 2021. Locally exact asymptotic homogenization of viscoelastic composites under anti-plane shear loading. Mech. Mater. 155, 103752.

Henkes, A., Wessels, H., Mahnken, R., 2022. Physics informed neural networks for continuum micromechanics. Comput. Methods Appl. Mech. Eng. 393, 114790.

Hessman, P.A., Welschinger, F., Hornberger, K., Böhlke, T., 2021. On mean field homogenization schemes for short fiber reinforced composites: Unified formulation, application and benchmark. Int. J. Solids Struct. 230–231, 111141.

Jiang, J., Wu, J., Chen, Q., Chatzigeorgiou, G., Meraghni, F., 2023. Physically informed deep homogenization neural network for unidirectional multiphase/multi-inclusion thermoconductive composites. Comput. Methods Appl. Mech. Eng. 409, 115972.

Linghu, J., Gao, W., Dong, H., Nie, Y., 2025. Higher-order multi-scale physics-informed neural network (HOMS-PINN) method and its convergence analysis for solving elastic problems of authentic composite materials. J. Comput. Appl. Math. 456, 116223.

Masi, F., Stefanou, I., 2022. Multiscale modeling of inelastic materials with Thermodynamics-based Artificial Neural Networks (TANN). Comput. Methods Appl. Mech. Eng. 398, 115190.

McClenny, L.D., Braga-Neto, U.M., 2023. Self-adaptive physics-informed neural networks. J. Comput. Phys. 474, 111722.

Mori, T., Tanaka, K., 1973. Average stress in matrix and average elastic energy of materials with misfitting inclusions. Acta Metall. 21, 571–574.

Nguyen-Thanh, V.M., Anitescu, C., Alajlan, N., Rabczuk, T., Zhuang, X., 2021. Parametric deep energy approach for elasticity accounting for strain gradient effects. Comput. Methods Appl. Mech. Eng. 386, 114096.

Pallicity, T.D., Böhlke, T., 2021. Effective viscoelastic behavior of polymer composites with regular periodic microstructures. Int. J. Solids Struct. 216, 167–181.

Pindera, M.-J., Khatam, H., Drago, A.S., Bansal, Y., 2009. Micromechanics of spatially uniform heterogeneous media: A critical review and emerging approaches. Compos. B Eng. 40, 349–378.

Raissi, M., Perdikaris, P., Karniadakis, G.E., 2019. Physics-informed neural networks: A deep learning framework for solving forward and inverse problems involving nonlinear partial differential equations. J. Comput. Phys. 378, 686–707.

Ren, X., Lyu, X., 2024. Mixed form based physics-informed neural networks for performance evaluation of two-phase random materials. Eng. Appl. Artif. Intel. 127, 107250.

Samaniego, E., Anitescu, C., Goswami, S., Nguyen-Thanh, V.M., Guo, H., Hamdia, K., Zhuang, X., Rabczuk, T., 2020. An energy approach to the solution of partial differential equations in computational mechanics via machine learning: Concepts, implementation and applications. Comput. Methods Appl. Mech. Eng. 362, 112790.

Soyarslan, C., Pradas, M., 2024. Physics-informed machine learning in asymptotic homogenization of elliptic equations. Comput. Methods Appl. Mech. Eng. 427, 117043.

Wang, G., Chen, Q., He, Z., Pindera, M.-J., 2018. Homogenized moduli and local stress fields of unidirectional nano-composites. Compos. B Eng. 138, 265–277.

Wang, G., Pindera, M.-J., 2016. Locally-exact homogenization theory for transversely isotropic unidirectional composites. Mech. Res. Commun. 78, 2–14.

Willis, J.R., 1977. Bounds and self-consistent estimates for the overall properties of anisotropic composites. J. Mech. Phys. Solids 25, 185–202.

Wu, J., Chen, Q., Jiang, J., Chatzigeorgiou, G., Meraghni, F., 2024. Adaptive deep homogenization theory for periodic heterogeneous materials. Compos. Struct. 340, 118171.

Wu, J., Jiang, J., Chen, Q., Chatzigeorgiou, G., Meraghni, F., 2023. Deep homogenization networks for elastic heterogeneous materials with two- and three-dimensional periodicity. Int. J. Solids Struct. 284, 112521.